

# A deep learning approach to extract internal tides scattered by geostrophic turbulence

Han Wang<sup>1\*</sup>, Nicolas Grisouard<sup>1</sup>, Hesam Salehipour<sup>2</sup>, Alice Nuz<sup>1†</sup>, Michael Poon<sup>1‡</sup>, and Aurélien L. Ponte<sup>3</sup>

<sup>1</sup>Department of Physics, University of Toronto, Ontario, Canada

<sup>2</sup>Autodesk Research, Ontario, Canada

<sup>3</sup>Ifremer, Plouzané, France

## Key Points:

- A deep conditional Generative Adversarial Network is trained to extract tidal components in SSH snapshots from an idealized model.
- The network can extract tidal signals accurately in a snapshot whose underlying dynamics are different from training data.
- Performance of the network degrades when extracting tidal signals entangled with higher turbulence energies.

---

\*Current address, School of Mathematics, University of Edinburgh, Edinburgh, UK

†Current address, Tandon School of Engineering, New York University, New York, USA

‡Current address, Department of Astronomy and Astrophysics, University of Toronto, Ontario, Canada

Corresponding author: Han Wang, [hannnwangus@gmail.com](mailto:hannnwangus@gmail.com)

**Abstract**

Extraction of internal tidal (IT) signals is central to the interpretation of Sea Surface Height (SSH) data. The increased spatial resolution of future wide-swath satellite missions poses a challenge for traditional harmonic analysis, due to prominent and unsteady wave-mean interactions at finer scales. However, the wide swaths will also produce spatially two-dimensional SSH snapshots, which allows us to treat IT extraction as an image translation problem for the first time. We design and train TITE, a conditional Generative Adversarial Network, which, given a snapshot of raw SSH from an idealized eddy simulation, generates a snapshot of the embedded IT component. We test it on data whose dynamical regimes are different from the data provided during training. Despite the diversity and complexity of data, it accurately extracts ITs in most individual snapshots considered and reproduces physically meaningful statistical properties. Predictably, TITE’s performance decreases with the intensity of the turbulent flow.

**Plain Language Summary**

Wide-swath satellite observations of Sea Surface Height (SSH) data at high spatial resolutions will be available in abundance thanks to advances of instrumental technologies. Embedded in the observed SSH are internal tides, a physical process that plays a crucial role in ocean circulation. As they are entangled with background currents and eddies, such tidal signals are challenging to extract. On the other hand, the wide satellite swaths provide new opportunities as they allow us to regard the observations as spatially two-dimensional. Here we treat the tidal extraction solely as an image translation problem. We train TITE, a deep neural net that, given a snapshot of a raw SSH signal, produces a “fake” snapshot of the tidal SSH signal that is meant to reproduce the original. The data we use in this article is generated by idealized numerical simulations. Once adapted to realistic data, the network has the potential to become a new tidal extraction tool for satellite observations. More broadly, successes in our experiments can inspire other applications of generative networks to disentangle dynamical components in data where classical analysis may fail.

**1 Introduction**

Internal tides (hereafter “ITs”) are inertia-gravity waves generated by the ocean large-scale (barotropic) tidal currents flowing over submarine topographic features. They play large roles in deep/upper ocean mixing (Munk & Wunsch, 1998; Whalen et al., 2020; Lien & Gregg, 2001; Lahaye et al., 2019; Garrett, 2003), altimetric inference of balanced flows (Fu & Ferrari, 2008), and detection of ocean temperature changes (Zhao, 2016). For decades, IT extraction has been conducted via harmonic analysis (Munk & Hasselmann, 1964; Munk & Cartwright, 1966; Cartwright & Ray, 1990). Current altimetry has a typical spatial resolution of  $O(100)$  km (Ballarotta et al., 2019), which is sufficient to retrieve mode-1 and some of the mode-2 IT wavelengths of semidiurnal tides, along with the dominant turbulent balanced motions (hereafter “TBMs”; see Ray & Zaron, 2011). At these scales, the coupling between ITs and TBMs is usually weak and therefore substantial portions of the ITs are phase-locked with astronomical forcings (Egbert & Ray, 2000; Zaron, 2017). Harmonic fits can retrieve such phase-locked signals, even if the time sampling is longer than the tidal period, provided that the time series is long enough to diagnose the aliased lower frequencies (Carrere et al., 2021).

When ITs become incoherent (i.e., their phase shift with respect to their generating astronomical tide becomes time-dependent) due to scatterings from TBMs or modulations of mean density profiles, techniques such as complex demodulation (Munk et al., 1965; Colosi & Munk, 2006), least-square fits (Cartwright & Ray, 1990), Lagrangian filtering (Shakespeare & Hogg, 2017) or combination with in-situ data (Geoffroy & Nylander, 2022) are useful if well-sampled time series are available. For satellite observa-

tions, this is sometimes indeed the case, especially with multi-satellite observations (Zaron, 2015).

However, such techniques yield increasingly poor performance as temporal sampling rates decrease. According to several studies (Ray & Zaron, 2011; Zaron, 2015, 2017; Nelson et al., 2019), between 15% and 45% of mode-1 semidiurnal tidal variances can not be identified via conventional harmonic analysis, with more recent estimates reporting larger fractions of incoherence. Starkly, using 17 years’ and 20 years’ global satellite observations respectively, Shriver et al. (2012) and Zhao et al. (2016) find apparent disappearances of mode-1 semidiurnal tidal signals in equatorial Pacific regions, which Buijsman et al. (2017) attribute to equatorial incoherence rather than dissipation, as echoed in the dominance of incoherent tidal variance reported in Zaron (2017) and Nelson et al. (2019). Improvements of incoherent tidal extraction are hence required to better identify spatial distributions of tidal dissipation, which is crucial for predicting tidal mixing (Whalen et al., 2020). Such challenges will be exacerbated in the next generation of satellite altimetry, in particular the Surface Water Ocean Topography (SWOT) mission. In addition to SWOT’s coarse sampling period of up to 21 days (Morrow et al., 2019), another complication arises from the improved spatial resolution of a few tens of km in wavelength (Morrow et al., 2019). At these smaller spatial scales, higher-mode ITs tend to become more incoherent (Ray & Zaron, 2011; Dunphy & Lamb, 2014; Shriver et al., 2012; Carrere et al., 2021) due to stronger couplings with the TBMs linked to the increased relative vorticity magnitudes (Bühler, 2014; Zaron & Egbert, 2014).

Attempts to circumvent time series information and focus on the spatial domain date back to at least Ray & Zaron (2011). New opportunities will arise in future altimeters from the availability of data along wide swaths (two 50 km-wide swaths, 20 km apart for SWOT) as opposed to current linear tracks. As a result, they will produce spatially two-dimensional (2D) images and it will be possible to regard the extraction of IT signals as an operation on 2D snapshots. Recently proposed methods rely on exploiting distinct wavenumber spectral signatures of TBMs and internal waves (Torres et al., 2019), empirical modal mapping methods (Egbert & Erofeeva, 2021), dynamical relations to surface density fields (Ponte et al., 2017), or on data assimilation techniques (Metref et al., 2020; Le Guillou et al., 2021). Our goal is to propose an alternative method based on a deep-learning, image processing method.

Indeed, several theoretical arguments indicate that valuable information is contained in the spatial distribution of SSH field. Statistically, internal tides are concentrated around tidal wavenumbers determined by the Sturm-Liouville problem (Gill & Adrian, 1982; Ray & Zaron, 2011; Zaron, 2017). Also, in the TBM component, kinetic energy and enstrophy transfer rates derived from SSH satisfy properties from classical turbulence theories (Khatri et al., 2018). Alternatively, ray tracing or triad resonance theories provide deterministic constraints in highly idealized cases (Savva & Vanneste, 2018; Ward & Dewar, 2010). To probe whether spatial information alone is enough to extract ITs in a deterministic fashion, we propose to regard the IT extraction solely as an image-to-image translation problem and to develop what we call the “Toronto Internal Tide Emulator” (TITE), a deep convolutional neural network that extracts the SSH signature induced by IT from a raw, instantaneous SSH map via pattern recognition. In general, we find TITE to perform well in most SSH snapshots generated from a set of idealized simulations.

## 2 Methods

### 2.1 Idealized data supporting TITE’s development

Data to support TITE’s development are snapshots from a set of idealized numerical simulations, where mode-1 ITs are forced at a fixed tidal period  $T$  (12 hours) to prop-

agate through TBMs created by a baroclinically unstable jet (Ponte & Klein, 2015; Ponte et al., 2020). The SSH signatures of TBMs in these simulations are generally larger than those induced by ITs, and exhibit a significant overlap in spatial scales at  $O(100)$  km with ITs. Spatial filtering is thus difficult, an issue that is also faced by satellite altimetry in oceanic regions such as the Gulf Stream or Drake Passage, where powerful TBMs exist (Rocha et al., 2016; Richman et al., 2012).

We run the model under five different initial meridional density contrasts. With increasing contrast, the baroclinic jet becomes more unstable and creates a more vigorous baroclinic eddy field. The spectra induced by these eddies follow a geostrophic turbulence law (Ponte & Klein, 2015; Charney, 1971), and are thus identified as TBMs. In ascending order of stationary surface kinetic energy levels of TBM (hereafter referred to as “turbulence levels”), we label the five simulations as T1 to T5. The mean normalized vorticities (absolute values of surface vertical vorticities normalized by the local Coriolis frequency) over the jet width increase from 0.06 to 0.14 from T1 to T5. We refer to Ponte & Klein (2015) for details on the numerical setup, and recapitulate the relevant information in Text S1 in the Supporting Information (SI).

IT snapshots are computed online via harmonic fits over time series that are  $2T$  long and sampled every 300 seconds, or  $T/144$ . For simplicity, we only study  $\eta_{\text{cos}}^{(\text{sim})}$ , the cosine component of ITs from the simulations, defined in the same way as Dunphy et al. (2017):

$$\eta_{\text{cos}}^{(\text{sim})}(x, y, t) = \frac{1}{T} \int_{t-2T}^t \eta(x, y, t') \cos\left(\frac{2\pi}{T}t'\right) dt', \quad (1)$$

where  $x, y$  are the zonal and meridional coordinates, respectively, and  $\eta$  denotes raw SSH. For each snapshot, we cut out three square panels covering three fixed latitudinal bands, labeled as “down-jet”, “mid-jet” and “up-jet”, as illustrated in Fig. 1. Here, the term “up-jet” denotes locations closer to the tidal forcing regions. One hundred snapshots are captured every  $4T$  for each simulation in T1-5, resulting in 1500 pairs of  $\{\eta, \eta_{\text{cos}}^{(\text{sim})}\}$  panels (5 runs, 3 latitudinal bands, and 100 snapshots) altogether.

## 2.2 Deep-learning algorithm designed to extract tidal signals

During the design of the TITE runs, we implicitly make four assumptions: (1) there is abundant spatial information, (2) all snapshots are statistically independent from each other in time, (3) a raw SSH functionally determines its IT component, but properties of the functional dependence are unknown, and (4) there exists abundant data where ITs are already extracted from the raw SSH. We discuss these assumptions at the end of this article.

TITE is based on a conditional Generative Adversarial Network (hereafter referred to as “cGAN”). As the name implies, a cGAN consists of two parts, namely, a conditional generator (hereafter “generator”) that learns how to manufacture a “fake” image that’s conditioned on an “input image”, and a discriminator that tries to determine if an image is “genuine” (i.e., paired to the input image in the training data), or fake (i.e., created by the generator). Either part is on its own a convolutional neural network, and during training, the two parts compete against each other to co-evolve (Mirza & Osindero, 2014; Goodfellow et al., 2014). We denote the cosine IT panels generated from TITE as  $\eta_{\text{cos}}^{(\text{gen})}$ ; following our notations, the *input* image would be  $\eta$ , the *genuine* image would be  $\eta_{\text{cos}}^{(\text{sim})}$ , and the *fake* image would be  $\eta_{\text{cos}}^{(\text{gen})}$ . As reflected in this general workflow, during training, other than the paired panels, no further information is given to TITE.

The particular cGAN TITE is derived from is called “pix2pix” (Isola et al., 2017), applications of which range from artistic creations (ml4a, 2017) to scientific problems such as remote sensing image classifications (Lebedev et al., 2018). Our codes are adapted from a TensorFlow Tutorial (Tensorflow, n.d.). We refer to Text S6 and S4 in the SI for

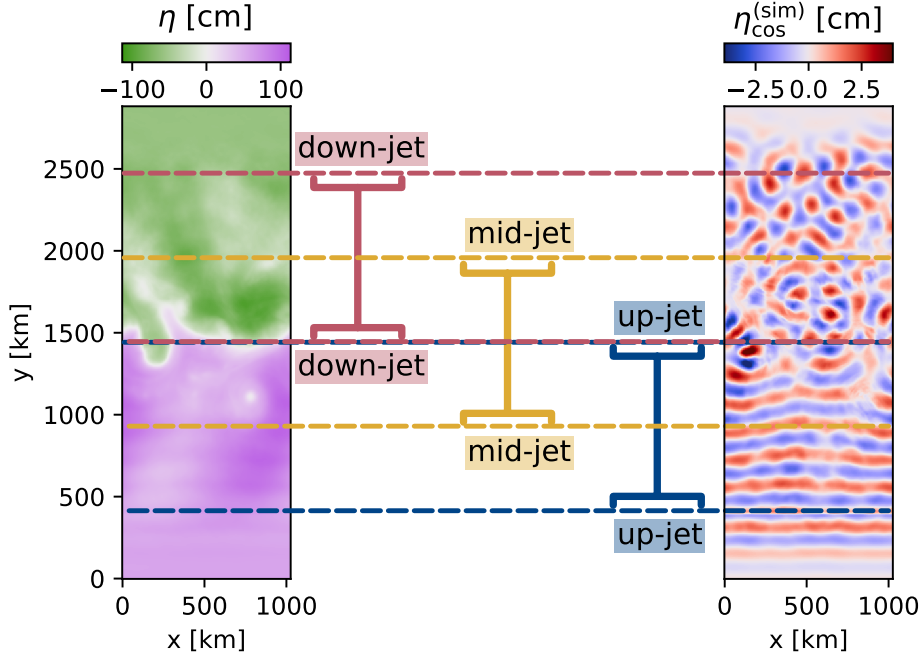


**Figure 1.** The “down-jet”, “mid-jet” and “up-jet” bands illustrated over a snapshot of  $\eta$  (left) and  $\eta_{\cos}^{(\text{sim})}$  (right), sampled from T3 at day 2120. The “mid-jet” band is centred around the baroclinic jet. ITs are forced to the south of “up-jet” bands, and as the ITs propagate northward and loses coherence due to interactions with the TBM, the  $\eta_{\cos}^{(\text{sim})}$  patterns are less reminiscent of plane waves in the “down-jet” band than in the “up-jet” band.

163 more details on our design considerations, and provide the code link in the Acknowledge-  
 164 ments. Here, we summarize the essential features.

165 The generator and the discriminator have around  $10^4$  and 2000 convolutional lay-  
 166 ers respectively. The considerable number of model parameters makes TITE a black box,  
 167 as in the case of many deep learning algorithms.

168 Prior to each epoch, training images are randomly reshuffled in time, cropped, flipped,  
 169 and rotated. Here, an epoch means the number of computations it takes for the cGAN  
 170 to iterate over all data in the training set once. The random cropping, rotation and flip-  
 171 ping are intended to introduce challenges that roughly mimic realistic situations where  
 172 we don’t have a priori knowledge of the observer’s orientation/location about IT gen-  
 173 eration sites, direction of propagation, and exact boundary conditions. By randomly reshuf-  
 174 fling in time, we enforce that every panel pair at every snapshot in the simulation be se-  
 175 quentially independent from the others. This means that any temporal information in  
 176 the simulations is unknown to the pix2pix kernel, in line with our assumption (2) made  
 177 previously in this section.

178 As the fully convolutional U-Net structure inherited from pix2pix in the genera-  
 179 tor can be applied to images of arbitrary sizes in principle, when producing Movies S1-  
 180 5 in the SI, we directly apply the trained TITE onto rectangular input images, even though  
 181 TITE is trained on square images illustrated in Fig. 1. This versatility on the shapes of  
 182 input images would be useful for along-swath satellite products.

183 We systematically run our code with TensorFlow 2.3.0 under Python 3.7. One hun-  
 184 dred training epochs with 960 pairs of  $\{\eta, \eta_{\text{cos}}^{(\text{sim})}\}$  in the training set take about 1.5 hours  
 185 with a NVIDIA GP100 GPU. For all the TITE runs in the article, we choose to present  
 186 the results after 600 training epochs. .

### 187 2.3 Division of data to training, testing and validation sets

188 As a first check on TITE’s performance, we randomly select 20% of all 1500 pairs  
 189 of  $\{\eta, \eta_{\text{cos}}^{(\text{sim})}\}$  panels from T1-5 to form a so-called validation set, and use the rest as the  
 190 training set. During training, TITE has access to all pairs of  $\{\eta, \eta_{\text{cos}}^{(\text{sim})}\}$  in the training  
 191 set, but none from the validation set. After 600 epochs, the training phase is over, and  
 192 we apply the trained TITE into snapshots in the validation set. The mean correlation  
 193 between  $\eta_{\text{cos}}^{(\text{sim})}$  and  $\eta_{\text{cos}}^{(\text{gen})}$  in the validation set turns out to be 0.85, which suggests that  
 194 the generated  $\eta_{\text{cos}}^{(\text{gen})}$  reasonably resemble the ground truths  $\eta_{\text{cos}}^{(\text{sim})}$ . However, under this  
 195 division, the training set contains turbulence levels that are statistically similar to the  
 196 validation set on which the trained TITE is applied, and the good correlation factors could  
 197 be caused by *overfitting*. Here, “overfitting” refers to a commonly accepted definition in  
 198 machine-learning contexts (Dietterich, 1995): a model is said to overfit when it tries to  
 199 fit the training data so closely that it does not generalize well to new data. To address  
 200 this possibility, we challenge TITE to extract  $\eta_{\text{cos}}^{(\text{sim})}$  signals linked to a *different* turbu-  
 201 lence level as those employed for its training.

202 Specifically, in what we refer to as the “ET1 run”, we reserve a *test* set, which con-  
 203 tains all 300 pairs of panels from the simulation T1 and *none* from T2, T3, T4 or T5.  
 204 Among the remaining panels from T2-5, we randomly select 80% pairs for the training  
 205 set, and reserve the other 20% for the validation set. The validation and test sets are  
 206 both inaccessible to TITE during training, but crucially, in terms of average turbulence  
 207 levels, the training set is similar to the validation set, yet *different* from the test set. This  
 208 procedure is designed to limit, or at least detect, the occurrence of overfitting. Simi-  
 209 larly, we carry out ET2-5 runs, following the same logic, where the test sets are panels  
 210 from the simulations T2-5 respectively.

## 211 3 Performance of TITE

212 As a graphical illustration, in Movie S1 in the SI, we re-order all the shuffled test  
 213 instances of ET1 in time. The reconstructed temporal information appears remarkable,  
 214 considering that the snapshots were randomly shuffled at the time of their generation  
 215 and hence that the temporal evolution of these images was unknown to TITE. However,  
 216 as turbulence level in test sets increases from ET2 to ET5, the evolution of  $\eta_{\text{cos}}^{(\text{gen})}$  bears  
 217 less and less resemblance with  $\eta_{\text{cos}}^{(\text{sim})}$  (Movies S2-5 in the SI). To find the underlying causes,  
 218 in this section, we evaluate the performance of TITE with several statistical metrics and  
 219 discuss the causes of relatively decreased performance when they arise. All metrics are  
 220 computed using standard methods and detailed in Text S5 in the SI .

221 We first investigate how close  $\eta_{\text{cos}}^{(\text{gen})}$  is to the ground truth  $\eta_{\text{cos}}^{(\text{sim})}$  by measuring the  
 222 correlation between the two, as in Torres et al. (2018). The mean correlation factors av-  
 223 eraged over all test instances in the ET1-5 runs are 0.91, 0.89, 0.83, 0.80 and 0.70, re-  
 224 spectively. The highly correlated predictions of TITE in the test set in ET1-4 are es-  
 225 pecially interesting, as turbulence levels of the test set are different from that of the train-  
 226 ing set. There is however a relatively sharper drop (from 0.80 to 0.70) in the mean cor-  
 227 relation from ET4 to ET5 in the test sets. Such a sharp drop can also be observed in  
 228 the histograms shown in the SI Fig. S7.

229 A few relevant snapshots from test sets are illustrated in Fig. 2. The first row presents  
 230 the snapshot with the highest correlation among all test sets in ET1-5. It belongs to ET1

231 and has a correlation factor of 0.95. The second and third row present the snapshot with  
 232 the lowest correlation among all test sets in ET5 and ET4, respectively. Judging by the  
 233 correlations, the worst case in ET4 has a correlation factor of 0.68, which is a significant  
 234 improvement over the correlation factor of 0.49 in the worst case in ET5. This agrees  
 235 with visual comparisons between the second and third rows in Fig. 2. This observation,  
 236 together with the sharp drop of mean correlation factors in ET5 noted above, suggest  
 237 a possible categoric difference between ET5 and ET1-4.

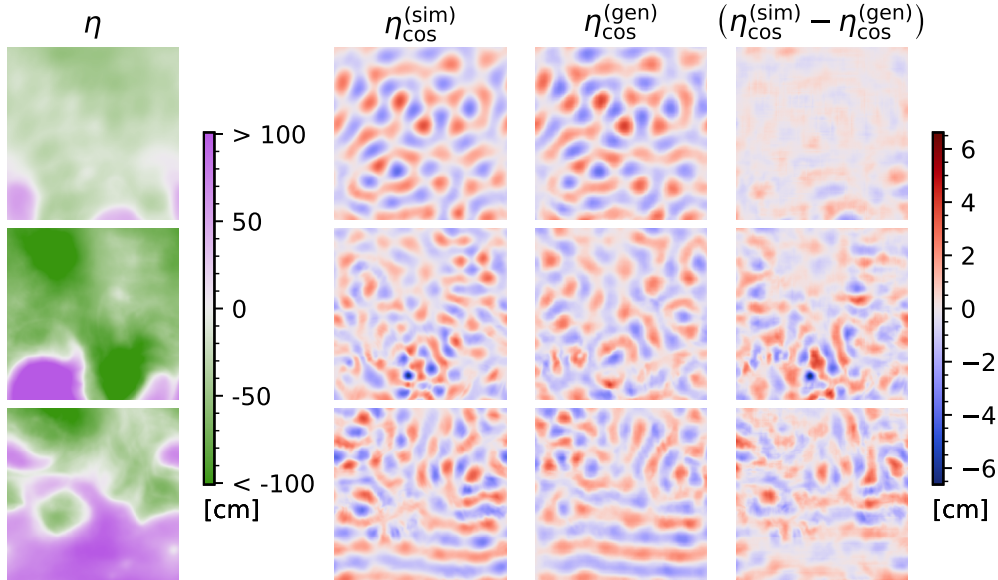


**Figure 2.** A few examples of individual tests. Top row: snapshot with the highest correlation among all sets (belongs to ET1). Middle and bottom rows: same for the lowest correlations among ET1-4, and ET1-5, respectively (belong to ET4 and 5, respectively). For legibility, we omit spatial axis labels, noting that the first, second, and third rows correspond to down-jet, down-jet, and mid-jet bands respectively; see Fig. 1 for their locations.

238 To gain more insight about the relative failures in ET5, we conduct a spectral anal-  
 239 ysis that focuses on comparing ET4 and ET5. The wavenumber spectra for the down-  
 240 jet and up-jet bands are computed separately for  $\eta_{\text{cos}}^{(\text{sim})}$  and  $\eta_{\text{cos}}^{(\text{gen})}$  in the test set of ET4  
 241 and ET5, and presented in Fig. 3. The spectra for mid-jet bands are omitted for read-  
 242 ability here and attached in Text S2 in the SI .

243 Prominent bumps appear near the wavenumbers corresponding to mode-1 tidal wave-  
 244 lengths in all the spectra of  $\eta_{\text{cos}}^{(\text{sim})}$  (Solid lines in Fig. 3). These bumps are somewhat broad,  
 245 and their locations are noticeably different between the down-jet and up-jet bands. This  
 246 is expected, as the density profiles and the Coriolis parameter both vary with latitude,  
 247 which modulates the mode-1 tidal wavelength. Such variations can also be found in satel-  
 248 lite observations (Ray & Zaron, 2011).

249 A qualitative difference can be found in the spectral behaviours between ET4 and  
 250 ET5. In ET4, the locations of spectral bumps in the  $\eta_{\text{cos}}^{(\text{gen})}$  spectra vary between the down-  
 251 jet and up-jet bands, in a manner such that they *closely* overlap with bumps of the  $\eta_{\text{cos}}^{(\text{sim})}$

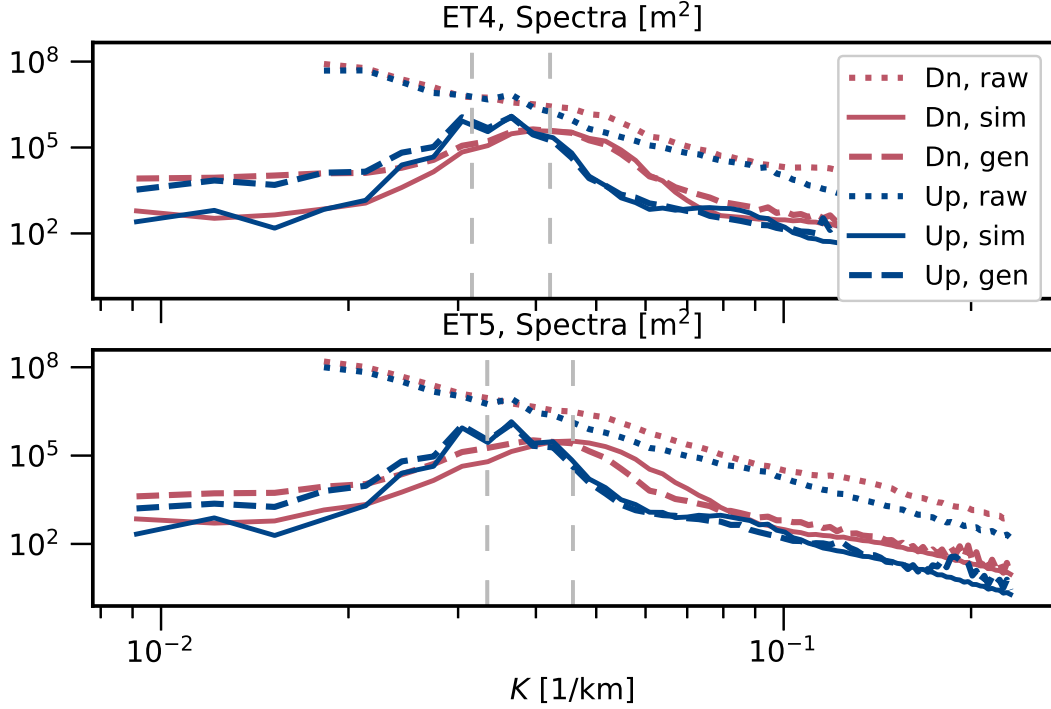


**Figure 3.** Spectra for the down-jet and up-jet bands in ET4 and ET5 test set. In the legends “Dn”, “Up” denote the down-jet and up-jet bands respectively. “raw”, “sim”, and “gen” denote spectra computed from panels of  $\eta$ ,  $\eta_{\cos}^{(\text{sim})}$ , and  $\eta_{\cos}^{(\text{gen})}$ , respectively. “ $K$ ” denotes the horizontal wavenumber magnitude. The vertical dashed lines mark the largest and smallest mode-1 tidal wavenumbers over the simulation domain at initial time. Raw spectra higher than  $2 \times 10^8 \text{m}^2$  at large scales are omitted. Higher wavenumbers are omitted.

252 spectra at both bands. This implies that in the ET4 run, the trained TITE identifies the  
 253 dominant wavelength even as it varies. In other words, TITE can identify patterns at  
 254 varying spatial scales. However, in the ET5 run, the  $\eta_{\cos}^{(\text{gen})}$  spectra *fail* to trace the lo-  
 255 cation of the bumps in the down-jet bands (dashed and solid red lines in lower panel of  
 256 Fig. 3). The performance in up-jet bands appears as good as ET4, which may be attributed  
 257 to the fact that the mode-1 tidal wavelengths to the south of the jets are the same in  
 258 all five simulations.

259 What causes the decrease of performance in ET5? We can formulate two possible  
 260 hypotheses: (i) the inherent difficulty of predicting increasingly complex patterns at higher  
 261 turbulence levels, and (ii) overfitting (see section 2.3 for its definition). Overall, we be-  
 262 lieve factor (i) affects TITE’s performance *more* than factor (ii), as we now argue.

263 In support of hypothesis (i), stronger scatterings of ITs from TBMs induce more  
 264 longitudinal variations as well as small-scale features in the IT components due to in-  
 265 creased incoherence. In addition, the tidal wavelengths vary more latitudinally due to  
 266 increased density gradients, which increases the diversity of dominant spatial scales of  
 267 IT signals across the domain and time. Both factors add complexities to the  $\eta$  and  $\eta_{\cos}^{(\text{sim})}$   
 268 patterns. As the turbulence levels increase from T1 to T5, the increased pattern complex-  
 269 ities in the test set pose more challenges to our algorithm, which explains the decreased  
 270 performance in ET5 in correlations and spectral behaviors.

271 The difficulty associated with vigorous turbulence levels is also reflected in the rel-  
 272 atively worse performance of TITE in the mid-jet bands centered around the turbulence.  
 273 We find that within each of ET1-5, the up-jet bands have a higher mean correlation than  
 274 the mid-jet bands, and as the turbulence level increases, this difference gets more pro-  
 275 nounced (See the histograms in Fig. S7 of the SI for quantitative behaviors). Spectral  
 276 behaviors degrade too, as detailed in Text S2 in the SI.

277 Turning our attention over to hypothesis (ii), in our experiments, overfitting may  
 278 provide a partial explanation for the performance degradation from ET4 to ET5. As ex-  
 279 pected from section 2.1, the kinetic energy and normalized vorticity for the TBM and  
 280 IT all increase from T1 to T5 (with the former increasing from  $0.04 \text{ m}^2/\text{s}^2$  to  $0.20 \text{ m}^2/\text{s}^2$ ).  
 281 In terms of these dynamical metrics, the training set of ET5 is less diverse compared to,  
 282 say, the training set of ET4 that spans a wider range of these metrics. Therefore, in ET5,  
 283 TITE may be fitting closely for turbulence levels in T1-4, and fails at T5 due to its mis-  
 284 match with T1-4, whereas in ET4, both T3 and T5 are included during training, and  
 285 a combination of T3 and T5 may impart some knowledge about T4 during testing.

286 However, several behaviours of TITE are inconsistent with the overfitting hypoth-  
 287 esis. First, if overfitting was the only factor, then during the test phase, TITE should  
 288 perform worse in ET1 than in ET2, as the range of dynamical metrics in ET1 is narrower  
 289 than in ET2. This does not turn out to be the case. In fact, the ET1 run produces the  
 290 best mean correlation in the test set among ET1-5. Second, compared to test sets, val-  
 291 idation sets are closer to training sets, and an overfitting model should perform better  
 292 in the validation sets than in the test sets. However, the mean correlations produced by  
 293 TITE in the test sets are higher than the validation sets by about 0.05 in ET1 and ET2.

294 On the other hand, hypothesis (i) provides better explanations for these disagree-  
 295 ments. In the ET1 test set, the turbulence levels are the lowest, and TITE performs well  
 296 despite the possible impacts from overfitting. In ET1 and ET2, the test data are at a  
 297 lower turbulence level than the validation data, and TITE generates better predictions.  
 298 Based on hypothesis (i), to improve TITE’s performance at higher turbulence levels, a  
 299 possible solution is to feed TITE with “overly turbulent” simulations during training,  
 300 as motivated by the better performances we have found in ET4, as compared to ET5.

## 301 4 Conclusions and Discussions

302 We designed a novel technique based on a deep neural network algorithm to ex-  
 303 tract internal tides that are entangled with geostrophic turbulence. We trained and val-  
 304 idated TITE using randomly shuffled simulation snapshots that were categorically dif-  
 305 ferent from the dynamic regime of the testing data. Due to lack of temporal informa-  
 306 tion, strong overlapping in spatial scales of ITs and TBMs, and incoherence, harmonic  
 307 fits or space filtering alone could not extract tidal signals accurately in the testing data  
 308 sets, and yet in most test cases, TITE can still (1) extract IT signals that agree well with  
 309 ground truths in a deterministic sense, and (2) capture the dominant tidal energy in the  
 310 wavenumber spectra, even when it varies temporally and latitudinally. When TITE does  
 311 not perform as well, the main cause seems to be the high complexities of the patterns  
 312 linked to stronger turbulent motions. Overall, we believe that this work provides a fresh  
 313 angle on how to disentangle dynamical components from two-dimensional data via a deep  
 314 learning approach. Some discussions are offered below.

315 Although we make no claim about TITE or cGANs in general as being the best  
 316 possible algorithms to specifically achieve our goal, we found it superior to other deep  
 317 learning methods we investigated, which include several types of decision trees regres-  
 318 sors, long short-term memory networks, and U-Net structures without a discriminator.  
 319 We did not attempt to optimize model parameters such as numbers of layers or learn-  
 320 ing rates, among others. Improvements on pix2pix such as that of Park et al. (2019) could

321 also improve our current implementation. Moreover, as mentioned in section 3, the gener-  
322 ated images contain spurious signals outside the dominant tidal bump, which remains  
323 to be resolved. We leave these as thoughts for future work.

324 So far, we have only applied TITE to the idealized simulations T1-5 with a sin-  
325 gular baroclinic jet and single tidal frequency, simplistic boundary conditions, flat topog-  
326 raphy, an absence of atmospheric forcings. As an ongoing work, we are investigating the  
327 effects of including snapshots from a global ocean GCM.

328 We used correlation factors and wavenumber spectra as main metrics in our eval-  
329 uations of TITE’s performance, similar to several other disentanglement efforts (Torres  
330 et al., 2019; Ponte et al., 2017). However, no direct physical meanings are attached to  
331 correlation factors, while no quantitative metric assessing spectral behaviours are widely  
332 adopted for practical applications. Our community has yet to widely adopt a skill met-  
333 ric to assess the accuracy of 2D tidal extraction.

334 With SWOT in mind, we may reassess the four assumptions stated in the first para-  
335 graph of section 2.2. All images used in this work have a 4 km horizontal resolution that  
336 resolves the tides adequately, addressing assumption (1). In preparation for satellite data  
337 that will suffer from measurement error and more limited resolutions, we may coarse-  
338 grain and augment the training data with the type of error expected in SWOT (Gaultier  
339 et al., 2016) to investigate their impacts. We could then rigorously compare TITE with  
340 other IT models (Carrere et al., 2021). Assumption (2), motivated by the incoherence  
341 of ITs and the relatively long sampling intervals of SWOT, is satisfied by the design of  
342 the TITE architecture, and by the frequent random shuffling of snapshots during train-  
343 ing. However, complete statistical independence between ITs and TBMs can be overly  
344 strict for several reasons, ranging from a higher temporal sampling at high latitude, to  
345 the possibility of “filling in the time gaps” with other sources of data such as those from  
346 assimilated models or in-situ instruments (d’Ovidio et al., 2019). From the overall sat-  
347 isfactory performance of TITE, assumption (3) appears to be satisfied in our simulation  
348 outputs, due to simulation design choices such as a perfectly harmonic incoming IT sig-  
349 nal, or simple boundary conditions. Under more realistic configurations, a functional de-  
350 pendence might not be guaranteed. On the other hand, assumption (3) can also be too  
351 strong a constraint, considering the known theoretical knowledge of IT/TBM interac-  
352 tions (Savva & Vanneste, 2018; Ward & Dewar, 2010). Assumption (4) relies on the premise  
353 that there will be pre-processed training data (presumably from highly skilled model out-  
354 puts) that mimic the dynamics to be sampled by SWOT. Productions of such data are  
355 receiving significant attention within the modelling communities (Zaron & Rocha, 2018;  
356 Rocha et al., 2016; Arbic et al., 2010; Savage et al., 2017). Overall, to make TITE even-  
357 tually applicable to SWOT and other satellite missions in the future, more work is re-  
358 quired, especially in coordination with different communities and perhaps combination  
359 with complementary methods.

## 360 Acknowledgments

361 We thank two anonymous reviewers for numerous constructive advice. H.W. and  
362 N.G. acknowledge the financial support of the Canadian Space Agency [14SUSWOTTO]  
363 and of the Natural Sciences and Engineering Research Council of Canada (NSERC) [RGPIN-  
364 2015-03684]. M.P. acknowledges support from the Summer Undergraduate Research Pro-  
365 gram of the Department of Physics at the University of Toronto. A.L.P. was supported  
366 by ANR project number 17-CE01-0006-01 and by project DIEGO of the CNES/TOSCA  
367 SWOT program. This work was made possible by the facilities of the Shared Hierarchi-  
368 cal Academic Research Computing Network (SHARCNET: [www.sharcnet.ca](http://www.sharcnet.ca)) and Com-  
369 pute/Calcul Canada. We have benefited from discussions with Laure Zanna, Brian K.  
370 Arbic, Michael W. Lever, Jason E. Summers, Jacques Vanneste and Ilia A. Iakovlev.

371 Simulation results corresponding to snapshots in T1-5 used in this study to train  
 372 and test TITE are published on Scholars Portal Dataverse (Ponte et al., 2020). Codes  
 373 defining the architecture of TITE are available at: [https://github.com/hannnwang/  
 374 Pix2PixTITEexamples](https://github.com/hannnwang/Pix2PixTITEexamples)

## 375 References

- 376 Arbic, B. K., Wallcraft, A. J., & Metzger, E. J. (2010). Concurrent simulation of the  
 377 eddy general circulation and tides in a global ocean model. *Ocean Modelling*,  
 378 *32*(3-4), 175–187.
- 379 Ballarotta, M., Ubelmann, C., Pujol, M.-I., Taburet, G., Fournier, F., Legeais, J.-F.,  
 380 ... others (2019). On the resolutions of ocean altimetry maps. *Ocean Science*,  
 381 *15*(4), 1091–1109.
- 382 Bühler, O. (2014). *Waves and Mean Flows* (2nd ed.). Cambridge: Cambridge  
 383 University Press. Retrieved from [http://ebooks.cambridge.org/ref/id/  
 384 CB09781107478701](http://ebooks.cambridge.org/ref/id/CB09781107478701) doi: 10.1017/CBO9781107478701
- 385 Buijsman, M. C., Arbic, B. K., Richman, J. G., Shriver, J. F., Wallcraft, A. J., &  
 386 Zamudio, L. (2017). Semidiurnal internal tide incoherence in the equatorial  
 387 pacific. *Journal of Geophysical Research: Oceans*, *122*(7), 5286–5305.
- 388 Carrere, L., Arbic, B. K., Dushaw, B., Egbert, G., Erofeeva, S., Lyard, F., ... Picot,  
 389 N. (2021, 1). Accuracy assessment of global internal-tide models using satellite  
 390 altimetry. *Ocean Science*, *17*, 147–180. doi: 10.5194/os-17-147-2021
- 391 Cartwright, D. E., & Ray, R. (1990). Oceanic tides from geosat altimetry. *Journal of  
 392 Geophysical Research: Oceans*, *95*(C3), 3069–3090.
- 393 Charney, J. G. (1971). Geostrophic turbulence. *Journal of the Atmospheric Sci-  
 394 ences*, *28*(6), 1087–1095.
- 395 Colosi, J. A., & Munk, W. (2006). Tales of the venerable honolulu tide gauge. *Jour-  
 396 nal of physical oceanography*, *36*(6), 967–996.
- 397 Dietterich, T. (1995). Overfitting and undercomputing in machine learning. *ACM  
 398 computing surveys (CSUR)*, *27*(3), 326–327.
- 399 Dunphy, M., & Lamb, K. G. (2014). Focusing and vertical mode scattering of the  
 400 first mode internal tide by mesoscale eddy interaction. *Journal of Geophysical Re-  
 401 search: Oceans*, *119*(1), 523–536.
- 402 Dunphy, M., Ponte, A. L., Klein, P., & Le Gentil, S. (2017). Low-mode internal tide  
 403 propagation in a turbulent eddy field. *Journal of Physical Oceanography*, *47*(3),  
 404 649–665.
- 405 d’Ovidio, F., Pascual, A., Wang, J., Doglioli, A. M., Jing, Z., Moreau, S., ... others  
 406 (2019). Frontiers in fine-scale in situ studies: Opportunities during the swot fast  
 407 sampling phase. *Frontiers in Marine Science*, *6*, 168.
- 408 Egbert, G., & Erofeeva, S. (2021). An approach to empirical mapping of incoherent  
 409 internal tides with altimetry data. *Geophysical Research Letters*, e2021GL095863.
- 410 Egbert, G., & Ray, R. (2000). Significant dissipation of tidal energy in the deep  
 411 ocean inferred from satellite altimeter data. *Nature*, *405*(6788), 775–778.
- 412 Fu, L.-L., & Ferrari, R. (2008). Observing oceanic submesoscale processes from  
 413 space. *Eos, Transactions American Geophysical Union*, *89*(48), 488–488.
- 414 Garrett, C. (2003). Internal tides and ocean mixing. *Science*, *301*(5641), 1858–1859.
- 415 Gaultier, L., Ubelmann, C., & Fu, L.-L. (2016). The challenge of using future swot  
 416 data for oceanic field reconstruction. *Journal of Atmospheric and Oceanic Tech-  
 417 nology*, *33*(1), 119–126.
- 418 Geoffroy, G., & Nycander, J. (2022). Global mapping of the nonstationary semid-  
 419 iurnal internal tide using argo data. *Journal of Geophysical Research: Oceans*,  
 420 e2021JC018283.
- 421 Gill, A. E., & Adrian, E. (1982). *Atmosphere-ocean dynamics* (Vol. 30). Academic  
 422 press.

- 423 Goodfellow, I., Pouget-Abadie, J., Mirza, M., Xu, B., Warde-Farley, D., Ozair, S.,  
 424 ... Bengio, Y. (2014). Generative adversarial nets. *Advances in neural informa-*  
 425 *tion processing systems*, 27.
- 426 Isola, P., Zhu, J.-Y., Zhou, T., & Efros, A. A. (2017). Image-to-image translation  
 427 with conditional adversarial networks. In *Proceedings of the IEEE conference on*  
 428 *computer vision and pattern recognition* (pp. 1125–1134).
- 429 Khatri, H., Sukhatme, J., Kumar, A., & Verma, M. K. (2018). Surface ocean en-  
 430 strophy, kinetic energy fluxes, and spectra from satellite altimetry. *Journal of*  
 431 *Geophysical Research: Oceans*, 123(5), 3875–3892.
- 432 Lahaye, N., Gula, J., & Rouillet, G. (2019). Sea surface signature of internal tides.  
 433 *Geophysical Research Letters*, 46(7), 3880–3890.
- 434 Lebedev, M., Vizilter, Y. V., Vygolov, O., Knyaz, V., & Rubis, A. Y. (2018).  
 435 Change detection in remote sensing images using conditional adversarial net-  
 436 works. *International Archives of the Photogrammetry, Remote Sensing & Spatial*  
 437 *Information Sciences*, 42(2).
- 438 Le Guillou, F., Lahaye, N., Ubelmann, C., Metref, S., Cosme, E., Ponte, A., ... Vi-  
 439 dard, A. (2021). Joint estimation of balanced motions and internal tides from  
 440 future wide-swath altimetry. *Journal of Advances in Modeling Earth Systems*,  
 441 e2021MS002613.
- 442 Lien, R.-C., & Gregg, M. (2001). Observations of turbulence in a tidal beam and  
 443 across a coastal ridge. *Journal of Geophysical Research: Oceans*, 106(C3), 4575–  
 444 4591.
- 445 Metref, S., Cosme, E., Le Guillou, F., Le Sommer, J., Brankart, J.-M., & Verron,  
 446 J. (2020). Wide-swath altimetric satellite data assimilation with correlated-error  
 447 reduction. *Frontiers in Marine Science*, 6, 822.
- 448 Mirza, M., & Osindero, S. (2014). Conditional generative adversarial nets. *arXiv*  
 449 *preprint arXiv:1411.1784*.
- 450 ml4a. (2017). *Machine Learning for Artists*. Retrieved from [https://ml4a.github](https://ml4a.github.io/guides/Pix2Pix/)  
 451 [.io/guides/Pix2Pix/](https://ml4a.github.io/guides/Pix2Pix/)
- 452 Morrow, R., Fu, L.-L., Ardhuin, F., Benkiran, M., Chapron, B., Cosme, E., ... oth-  
 453 ers (2019). Global observations of fine-scale ocean surface topography with the  
 454 surface water and ocean topography (swot) mission. *Frontiers in Marine Science*,  
 455 6, 232.
- 456 Munk, W., & Cartwright, D. E. (1966). Tidal spectroscopy and prediction. *Philo-*  
 457 *sophical Transactions of the Royal Society of London. Series A, Mathematical and*  
 458 *Physical Sciences*, 259(1105), 533–581.
- 459 Munk, W., & Hasselmann, K. (1964). Super-resolution of tides. *Studies on oceanog-*  
 460 *raphy*, 339–344.
- 461 Munk, W., & Wunsch, C. (1998). Abyssal recipes ii: Energetics of tidal and wind  
 462 mixing. *Deep Sea Research Part I: Oceanographic Research Papers*, 45(12), 1977–  
 463 2010.
- 464 Munk, W., Zetler, B., & Groves, G. (1965). Tidal cusps. *Geophysical Journal Inter-*  
 465 *national*, 10(2), 211–219.
- 466 Nelson, A. D., Arbic, B. K., Zaron, E. D., Savage, A. C., Richman, J. G., Buijsman,  
 467 M. C., & Shriver, J. F. (2019). Toward realistic nonstationarity of semidiur-  
 468 nal baroclinic tides in a hydrodynamic model. *Journal of Geophysical Research:*  
 469 *Oceans*, 124(9), 6632–6642.
- 470 Park, T., Liu, M.-Y., Wang, T.-C., & Zhu, J.-Y. (2019). Semantic image synthesis  
 471 with spatially-adaptive normalization. In *Proceedings of the IEEE/CVF conference on*  
 472 *computer vision and pattern recognition* (pp. 2337–2346).
- 473 Ponte, A. L., & Klein, P. (2015). Incoherent signature of internal tides on sea level  
 474 in idealized numerical simulations. *Geophysical Research Letters*, 42(5), 1520–  
 475 1526.
- 476 Ponte, A. L., Klein, P., Dunphy, M., & Le Gentil, S. (2017). Low-mode internal tides

- 477 and balanced dynamics disentanglement in altimetric observations: Synergy with  
 478 surface density observations. *Journal of Geophysical Research: Oceans*, *122*(3),  
 479 2143–2155.
- 480 Ponte, A. L., Le Gentil, S., & Grisouard, N. (2020). *Internal tides and geostrophic*  
 481 *turbulence in a Boussinesq re-entrant channel*. Scholars Portal Dataverse. Re-  
 482 trieved from [https://doi.org/10.5683/SP2/](https://doi.org/10.5683/SP2/HU58SG)  
 483 [HU58SG](https://doi.org/10.5683/SP2/HU58SG) doi: 10.5683/SP2/  
 484 HU58SG
- 484 Ray, R. D., & Zaron, E. D. (2011). Non-stationary internal tides observed with  
 485 satellite altimetry. *Geophysical Research Letters*, *38*(17).
- 486 Richman, J. G., Arbic, B. K., Shriver, J. F., Metzger, E. J., & Wallcraft, A. J.  
 487 (2012). Inferring dynamics from the wavenumber spectra of an eddying global  
 488 ocean model with embedded tides. *Journal of Geophysical Research: Oceans*,  
 489 *117*(C12).
- 490 Rocha, C. B., Chereskin, T. K., Gille, S. T., & Menemenlis, D. (2016). Mesoscale to  
 491 submesoscale wavenumber spectra in drake passage. *Journal of Physical Oceanog-*  
 492 *raphy*, *46*(2), 601–620.
- 493 Savage, A. C., Arbic, B. K., Alford, M. H., Ansong, J. K., Farrar, J. T., Menemenlis,  
 494 D., ... others (2017). Spectral decomposition of internal gravity wave sea sur-  
 495 face height in global models. *Journal of Geophysical Research: Oceans*, *122*(10),  
 496 7803–7821.
- 497 Savva, M. A., & Vanneste, J. (2018). Scattering of internal tides by barotropic  
 498 quasigeostrophic flows. *Journal of Fluid Mechanics*, *856*, 504–530.
- 499 Shakespeare, C. J., & Hogg, A. M. (2017). Spontaneous surface generation and in-  
 500 terior amplification of internal waves in a regional-scale ocean model. *Journal of*  
 501 *Physical Oceanography*, *47*(4), 811–826.
- 502 Shriver, J., Arbic, B. K., Richman, J., Ray, R., Metzger, E., Wallcraft, A., & Timko,  
 503 P. (2012). An evaluation of the barotropic and internal tides in a high-resolution  
 504 global ocean circulation model. *Journal of Geophysical Research: Oceans*,  
 505 *117*(C10).
- 506 Tensorflow. (n.d.). *pix2pix: Image-to-image translation with a conditional GAN*.  
 507 Retrieved from <https://www.tensorflow.org/tutorials/generative/pix2pix>  
 508 (Accessed on Sep.20, 2020.)
- 509 Torres, H., Klein, P., Menemenlis, D., Qiu, B., Su, Z., Wang, J., ... Fu, L.-L.  
 510 (2018). Partitioning ocean motions into balanced motions and internal gravity  
 511 waves: A modeling study in anticipation of future space missions. *Journal of*  
 512 *Geophysical Research: Oceans*, *123*(11), 8084–8105.
- 513 Torres, H., Klein, P., Siegelman, L., Qiu, B., Chen, S., Ubelmann, C., ... Fu, L.-L.  
 514 (2019). Diagnosing ocean-wave-turbulence interactions from space. *Geophysical*  
 515 *Research Letters*, *46*(15), 8933–8942.
- 516 Ward, M. L., & Dewar, W. K. (2010). Scattering of gravity waves by potential vor-  
 517 ticity in a shallow-water fluid. *Journal of fluid mechanics*, *663*, 478–506.
- 518 Whalen, C. B., de Lavergne, C., Garabato, A. C. N., Klymak, J. M., Mackinnon,  
 519 J. A., & Sheen, K. L. (2020). Internal wave-driven mixing: governing processes  
 520 and consequences for climate. *Nature Reviews Earth & Environment*, *1*(11),  
 521 606–621.
- 522 Zaron, E. D. (2015). Nonstationary internal tides observed using dual-satellite al-  
 523 timetry. *Journal of Physical Oceanography*, *45*(9), 2239–2246.
- 524 Zaron, E. D. (2017). Mapping the nonstationary internal tide with satellite altime-  
 525 try. *Journal of Geophysical Research: Oceans*, *122*(1), 539–554.
- 526 Zaron, E. D., & Egbert, G. D. (2014, 2). Time-variable refraction of the internal tide  
 527 at the hawaiian ridge. *Journal of Physical Oceanography*, *44*, 538–557. Retrieved  
 528 from <http://journals.ametsoc.org/doi/abs/10.1175/JPO-D-12-0238.1> doi:  
 529 10.1175/JPO-D-12-0238.1
- 530 Zaron, E. D., & Rocha, C. B. (2018). Internal gravity waves and meso/submesoscale

- 531 currents in the ocean: anticipating high-resolution observations from the swot  
532 swath altimeter mission. *Bulletin of the American Meteorological Society*, 99(9),  
533 ES155–ES157.
- 534 Zhao, Z. (2016). Internal tide oceanic tomography. *Geophysical Research Letters*,  
535 43(17), 9157–9164.
- 536 Zhao, Z., Alford, M. H., Girton, J. B., Rainville, L., & Simmons, H. L. (2016).  
537 Global observations of open-ocean mode-1 m2 internal tides. *Journal of Physical*  
538 *Oceanography*, 46(6), 1657–1684.